Cell Reports
Physical Science

CellPress
OPEN ACCESS

Article

Efficient indoor light harvesting with $CH_3NH_3Pb(I_{0.8}Br_{0.2})_3$ solar modules and sodium-ion battery

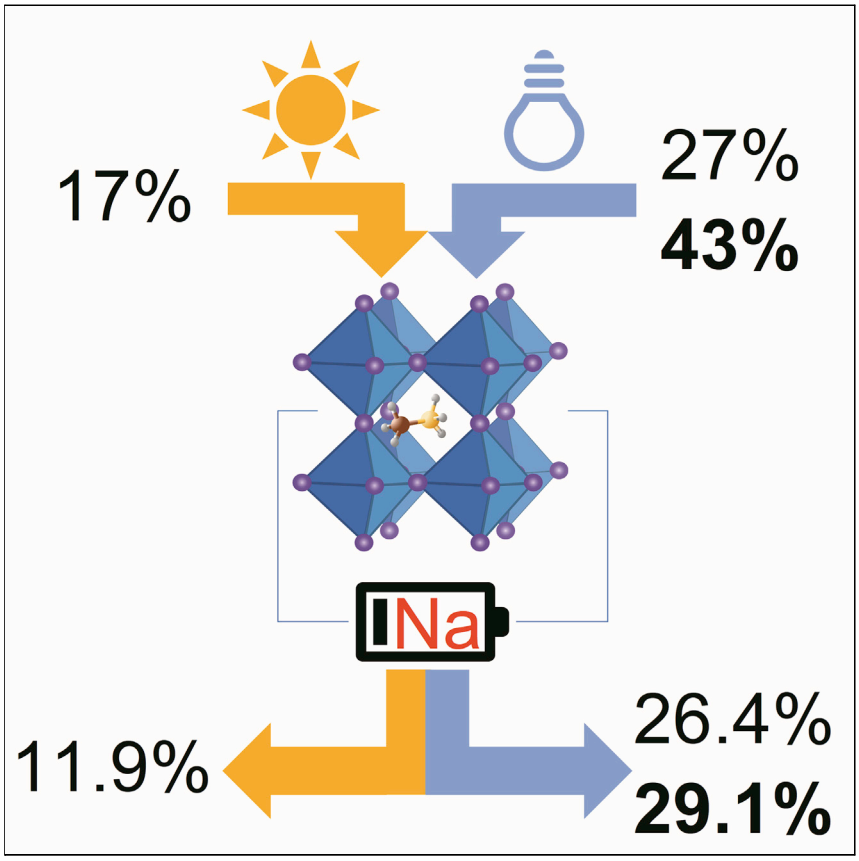

Abundant, efficient, and safe power sources for small indoor distributed sensors are still not a reality. Kin et al. demonstrate the efficient charging of a sodium-ion battery and high-voltage perovskite solar module under indoor LED light to fill this niche that is immune to damage from charging under the sun.

Li-Chung Kin, Zhifa Liu, Oleksandr Astakhov, ..., Rüdiger-A Eichel, Uwe Rau, Tsvetelina Merdzhanova

l.kin@fz-juelich.de (L.-C.K.)
t.merdzhanova@fz-juelich.de (T.M.)

Highlights

High-efficiency wide-band-gap lead halide perovskite under LED illumination

High efficiency direct charging under one-sun and LED illumination with sodium-ion battery

Wide range of illumination intensities demonstrated

Design principles for safe and efficient direct PV-battery integration demonstrated

Kin et al., Cell Reports Physical Science 3, 101123
November 16, 2022
https://doi.org/10.1016/j.xcrp.2022.101123

Please cite this article in press as: Kin et al., Efficient indoor light harvesting with $CH_3NH_3Pb(I_{0.8}Br_{0.2})_3$ solar modules and sodium-ion battery, Cell Reports Physical Science (2022), https://doi.org/10.1016/j.xcrp.2022.101123

Cell Reports
Physical Science

Article

Efficient indoor light harvesting with $CH_3NH_3Pb(I_{0.8}Br_{0.2})_3$ solar modules and sodium-ion battery

Li-Chung Kin,[1,2,6,*] Zhifa Liu,[1,6] Oleksandr Astakhov,[1] Sergey Shcherbachenko,[1] Hans Kungl,[3] Thomas Kirchartz,[1,4] Rüdiger-A Eichel,[3,5] Uwe Rau,[1,2] and Tsvetelina Merdzhanova[1,7,*]

SUMMARY

Wide-band-gap perovskite solar cells are a good spectral match to indoor lighting and have the potential for high-efficiency indoor energy harvesting. A perovskite-charged battery is shown to operate at both one-sun and indoor lighting conditions with high efficiency. We demonstrate energy harvesting and storage from 300 lux to AM1.5G illumination realized using wide-band-gap lead halide perovskite ($CH_3NH_3Pb(I_{0.8}Br_{0.2})_3$) modules directly coupled to a high-rate-capable sodium-ion battery ($NaTi_2(PO_4)_2$@CNF/1M $NaPF_6$ in diglyme/Na) without power electronics. We show a high power conversion efficiency (PCE) of 43.9% for perovskite solar modules under high-intensity LED illumination (24.5 $mWcm^{-2}$), 31% PCE under 500 lux light-emitting diode (LED) illumination, and an overall efficiency of 26.4%. The present setup could form the foundation of future indoor light-harvesting solutions for internet-of-things devices and sensors.

INTRODUCTION

Indoor energy harvesting has always faced the pressures of being intermittent, low powered, and far more complex and expensive than simply putting in a battery. With the increasing use of indoor light-emitting diode (LED) lighting,[1] matching the LED output spectrum with the absorption spectrum of lead halide perovskite solar cells creates an opportunity to reuse emitted light with high efficiency to power infrequently used devices or low-powered sensors such as e-ink displays[2] or infrared (IR) sensors. An indoor photovoltaic (PV) light harvester will still struggle to directly deliver stable power for electronics due to the low light intensities in indoor environments. One way around this problem is to attach energy storage to the light harvester, collecting stray light over a long time and providing power when needed in shorter and higher bursts.[3,4]

In our recent studies,[5,6] we compared different PV technologies under different lighting conditions and show improved performance of the thin-film silicon solar cells under artificial illumination due to much better spectral matching. The solar spectrum contains a substantial fraction of infrared photons that imply that ideal PV band gaps are in the near infrared between 1.1 and 1.45 eV.[7] LED-based indoor illumination, however, has little to no contributions of infrared photons, which implies a blue shift of the optimal band gap toward 1.7 to 2.0 eV depending on the type and spectrum of the LED.[8] Therefore, classical crystalline Si solar cells with a band gap of 1.12 eV are not ideal for indoor PVs. Various organic as well as halide-perovskite solar cells have both high efficiencies under outdoor illumination

[1]Institut für Energie- und Klimaforschung (IEK-5), Forschungszentrum Jülich GmbH, 52428 Jülich, Germany

[2]Faculty of Electrical Engineering and Information Technology, RWTH Aachen University, Mies-van-der-Rohe-Straße 15, 52074 Aachen, Germany

[3]Fundamental Electrochemistry (IEK-9), Forschungszentrum Jülich GmbH, 52428 Jülich, Germany

[4]Faculty of Engineering and CENIDE, University of Duisburg-Essen, Carl-Benz-Str. 199, 47057 Duisburg, Germany

[5]Institute of Physical Chemistry, RWTH Aachen University, Landoltweg 2, 52074 Aachen, Germany

[6]Senior author

[7]Lead contact

*Correspondence: l.kin@fz-juelich.de (L.-C.K.), t.merdzhanova@fz-juelich.de (T.M.)

https://doi.org/10.1016/j.xcrp.2022.101123

Please cite this article in press as: Kin et al., Efficient indoor light harvesting with $CH_3NH_3Pb(I_{0.8}Br_{0.2})_3$ solar modules and sodium-ion battery, Cell Reports Physical Science (2022), https://doi.org/10.1016/j.xcrp.2022.101123

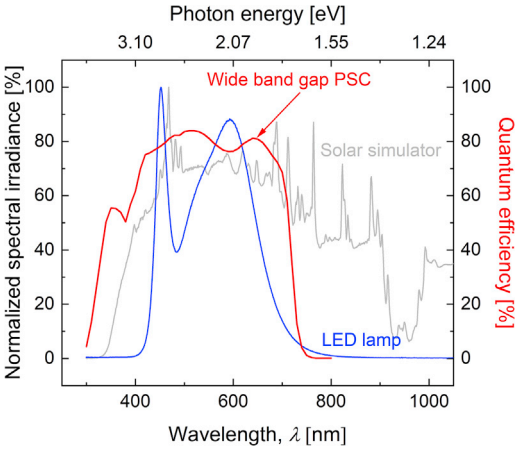

Figure 1. Irradiance spectra overlaid with solar cell quantum efficiency

Normalized spectral irradiance versus wavelength spectrum of an LED lamp (4,000 K, cool white) and an AM1.5G solar simulator, overlaid with the external quantum efficiency (EQE) of a wide-band-gap perovskite ($CH_3NH_3Pb(I0._8Br0._2)_3$) solar cell with CMC:ICBA electron transfer layer.

and substantially higher band gaps than crystalline Si.[9–14] However, given the offset between the optimal band gaps for outdoor (AM1.5G) illumination and LED-based indoor illumination, device optimization is still mostly done for lower band gaps. Highly efficient solar cells with band gaps in the 1.7 to 2 eV range are substantially more difficult to find than high efficiencies in the region between 1.5 and 1.6 eV that includes most highly efficient perovskites.[9,15] Thus, while there have been substantial achievements reported recently in the field of indoor PVs with solution-processable thin-film solar cells,[16–18] there may still be room for further improvement.

In order to improve efficiencies and, in particular, open-circuit voltages of halide perovskite solar cells, we have recently shown how the use of lead acetate as a precursor combined with the right choice of contact materials can substantially reduce bulk and interface recombination. We realized $CH_3NH_3PbI_3$-based devices with open-circuit voltages of 1.26 V at a band gap of 1.6 eV[19] using a combination of lead acetate and lead chloride precursors. The material showed exceptionally long charge-carrier lifetimes even in the presence of interfaces.[20,21] By including CH_3NH_3Br, we could further increase the band gap to 1.72 eV and achieve open-circuit voltages of 1.35 V,[22] which are the highest reported so far for a band gap around 1.7 eV under standard test conditions. Here, we make use of these findings and create three-cell minimodules based on the previously published solar cell recipe. The wide band gap allows an efficient overlap with the used LED spectrum (commercial "4,000 K" LED, cool white) as shown in Figure 1 and is close to the optimum band gap for indoor illumination as discussed in the literature.[8,23,24] This good overlap would result in good spectrum utilization with low thermalization losses under LED illumination.

The use of PVs to charge batteries requires modules of series-connected cells or a boost converter,[3,25] as the charging voltage of a battery typically exceeds the open-circuit voltage of a single solar cell. Recent charging of batteries using perovskite solar cells (PSCs) under AM1.5G illumination includes efforts utilizing a series of 4 perovskite cells (12.44%[26] and 12.65%[27] PCE), connected to a lithium-ion battery directly for 9.25%[26] and 7.8%[27] overall (round-trip) efficiency. Others have also successfully demonstrated direct coupling of other battery chemistries such as Zn-ion (12.92% PCE, 6.4% overall efficiency)[28] and Al-ion (18.5% PCE, 12.04% overall)[29] under one-sun, while efforts to use cells connected to converters reached one-sun

Please cite this article in press as: Kin et al., Efficient indoor light harvesting with $CH_3NH_3Pb(I_{0.8}Br_{0.2})_3$ solar modules and sodium-ion battery, Cell Reports Physical Science (2022), https://doi.org/10.1016/j.xcrp.2022.101123

solar-to-battery charging efficiency of 14.9% and overall efficiency of 9.9%, respectively.[25]

Indoor illumination power densities, however, are typically in the μW range and pose a challenge for the use of boost converters that typically draw a minimum of 0.5–2 mW in power, necessitating direct coupling of the PV to batteries to avoid relatively large converter losses. To date, only a few studies have focused on PSC modules under LED illumination,[17,30–32] and much less have shown that the high efficiencies of PSCs promised under LED illumination can be put to usable work for charging devices or running electronics.

Furthermore, the performance of a PSC under one-sun illumination has rapidly improved with highest certified PSC efficiencies under AM1.5G illumination at 25.4%[14] and mini modules reaching 19.3%.[33,34] Furthermore, with efficiencies under indoor illumination regularly exceeding 30%,[17,35,36] we can reasonably expect upwards of 20% overall efficiency for LED-illuminated charging, yet such values have not been demonstrated thus far.[37] There is also currently no fixed standard for reporting LED-light-illuminated power conversion efficiency, and there is a cursory trend in recent papers that seems to point to higher lux values corresponding to higher efficiencies above 30%,[35] but this trend has not been described yet.

In our previous work, we demonstrated the theoretical feasibility of the unaided operation with directly coupled PV and battery devices with a high degree of power coupling—that PV operation will be close to optimal.[38] In this work, we use this approach and tailor a perovskite pseudo-module to match the battery voltage under target irradiance conditions at the office illumination of 300–500 lux.[39] Combined with our previous work on high-rate-capable sodium-ion batteries,[40] we were able to keep load characteristics more or less constant throughout the whole range of intensities, including under AM1.5G illumination.

Here, we demonstrate high-efficiency directly coupled light harvesting under AM1.5G illumination using a wide-band-gap perovskite module and a high-rate-capable sodium battery. The harvested energy at every level of illumination is discharged across a fixed resistor to demonstrate that the harvested power can be put to useful work. We achieved overall efficiencies in excess of 20% under LED illumination and 11.5% overall efficiency under AM1.5G illumination.

RESULTS

Perovskite module characterization

The cells used in our work are inverted p-i-n cells based on the layer stack glass/ITO/PTAA/$CH_3NH_3Pb(I_{0.8}Br_{0.2})_3$/ETL/BCP/Ag, where ITO is indium tin oxide, PTAA is poly(triarylamine), BCP is bathocuproine, and ETL is an electron transfer layer: C_{60}-fused *N*-methylpyrrolidine-m-C_{12}-phenyl (CMC)[41,42] and indene-C_{60} bisadduct (ICBA),[43] which are mixed in a 1:1 ratio. The preparation of cells is based on using a prepatterned glass/ITO substrate on which PTAA and the perovskite and ETL layer are spin coated, whereas BCP and Ag are evaporated. This CMC:ICBA blend has been shown previously to lead to the highest open-circuit voltages for a PSC in that band-gap range (1.72 eV) and an excellent energy level alignment to the $CH_3NH_3Pb(I_{0.8}Br_{0.2})_3$ absorber layer.[22]

For the experiment a special arrangement has been used to emulate a 0.48 cm^2 three-cell modules by connecting three 0.16 cm^2 cells via a printed circuit board

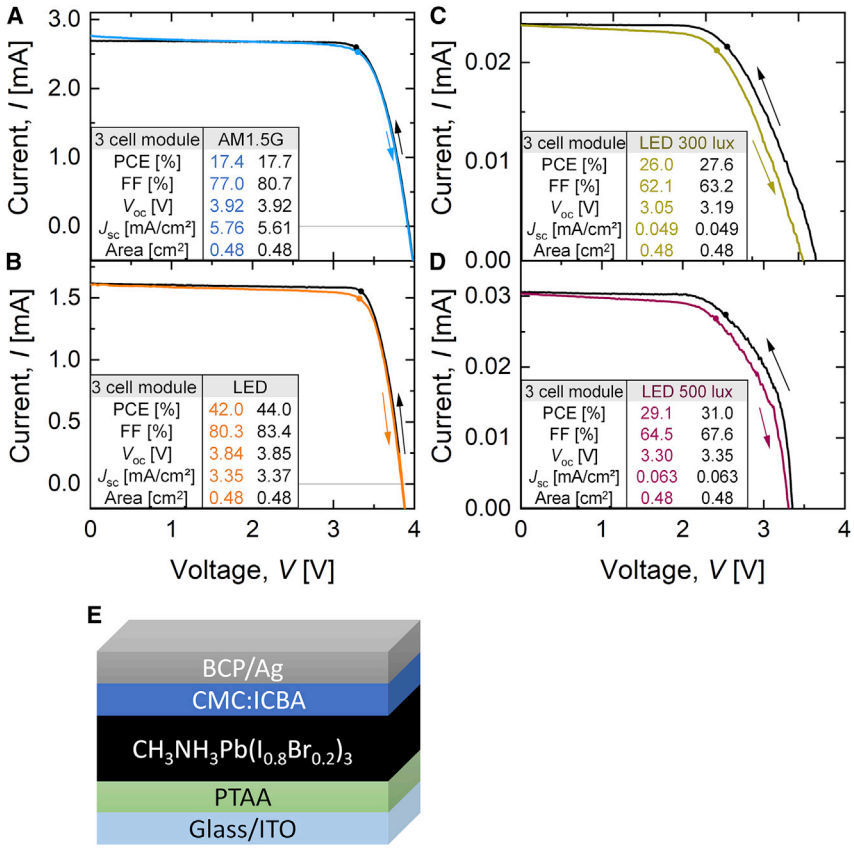

Figure 2. Illuminated current voltage curves for the $CH_3NH_3Pb(I_{0.8}Br_{0.2})_3$ module

(A) Under AM1.5G conditions (black, reverse scan and light blue, forward scan) with layer stack in inset.

(B) Unfiltered concentrated LED illumination (24.5 $mWcm^{-2}$) (black, reverse scan, orange forward scan).

(C) Filtered LED illumination under 300 lux LED illumination (black reverse scan, gold forward scan).

(D) Filtered LED illumination under 500 lux LED illumination (black reverse scan, maroon forward scan).

(E) Layer stack.

and gold-plated spring pins. Doing so enabled the quick fabrication of modules from previously tested cells.[19] Our three-cell module had a PCE of 17.7%, a fill factor of 80.7%, a J_{sc} of 5.61 $mAcm^{-2}$, and a V_{oc} of 3.92 V under AM1.5G illumination (Figure 2A) and a PCE of 44.0%, a fill factor of 83.4%, a J_{sc} of 3.37 $mAcm^{-2}$, and a V_{oc} of 3.85 V under concentrated LED (24.5 mW cm^{-2}; Figures 2B). Under filtered LED illumination (300 lux; Figure 2C), we have PCE of 27.6%, a fill factor of 63.2%, a J_{sc} of 0.0496 $mAcm^{-2}$, and a V_{oc} of 3.19 V. Under filtered LED illumination (500 lux; Figure 2D), we have PCE of 31.0%, a fill factor of 67.6%, a J_{sc} of 0.0638 $mAcm^{-2}$, and a V_{oc} of 3.35 V. The layer stack is shown in Figure 2E. Individual current-voltage (IV) curves for the other illumination intensities and more information regarding the PSCs can be found in Figures S1–S3, S8, and S9 and Table S1.

The initial array of four cells was connected in parallel and shared front-side contacts via two tracts of ITO deposited onto the glass and silver contact strips straddling the ITO strips. Individual rear contacts were made by evaporating silver, and active areas were defined by the overlapping areas of front and rear contacts. By cutting the ITO tracts in half between the front contacts and separating the silver rear contact strips

Please cite this article in press as: Kin et al., Efficient indoor light harvesting with $CH_3NH_3Pb(I_{0.8}Br_{0.2})_3$ solar modules and sodium-ion battery, Cell Reports Physical Science (2022), https://doi.org/10.1016/j.xcrp.2022.101123

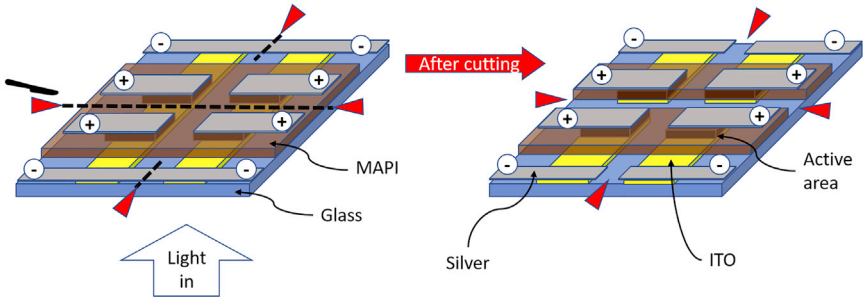

Figure 3. Solar module cut scheme

Cut scheme to modify the as deposited 4 × 0.16 cm^2 arrays into individual cells by cutting with a scalpel. Red arrows for reference to indicate areas cut. Three of the four cells were then connected in series to form the module.

connecting them (Figure 3), the array of parallel cells could be separated into four distinct cells, of which three were connected to form the required module for better voltage matching with the battery.

Sodium-ion battery characterization

Sodium-ion batteries were made with sodium titanium phosphate cathode, metallic sodium anode and diglyme (diethylene glycol dimethyl ether [DEGDME]) electrolyte. Sodium titanium phosphate ($NaTi_2(PO_4)_2$ [NTP]) was coated onto sheets of carbon nano-felt (NTP@CNF), and metallic sodium electrodes were chosen due to their high charge-rate capability,[44] low charge-discharge overpotential, and distinct charge- and discharge-voltage plateau.[40] Here, we used 1 M $NaPF_6$ in diglyme electrolyte for stability and high ionic conductivity[45,46] and a glass fiber separator. In Figure 4A, we see the charge-discharge curve of the sodium-ion batteries that were used for the experiment, which shows a very distinct charge plateau up to 5 C-rate, and in Figure 4B, we see the discharge and specific discharge capacity under varying charge-discharge rates of up to 10 mA. Under LED illumination, charge rates correspond to an approximately 1.5 C-rate (1.3 mA) at maximum LED illumination (~24.5 mW cm^{-2}) and below a 0.2 C-rate at 300 lux. Under AM1.5G illumination, charge rates correspond to an approximately 2.3 C-rate (2.8 mA).

PV-battery charge-discharge setup

To test the perovskite modules for indoor battery charging under LED lighting, we set up our system as shown in Figure 5. In Figure 5, the perovskite modules are contacted via gold pins on a printed circuit board (PCB), which connects three of the four cells in series within an airtight box (data not shown). Three of the four cells were connected into a module to better match the voltage of the battery. The wires are then fed out to the measurement circuit and battery via wires connected to the circuit board. Neutral density filters were used to attenuate the LED light intensity down to 300 lux. The same setup is used with AM1.5G illumination instead of the LED bulb. Table 1 shows the relevant intensities in lux and SI (Système International) units for the points measured under the charge-discharge setup, while the normalized corresponding spectra for these points can be found in Figure S4.

Metrics for the operation of the combined PV-battery system

The coupling factor

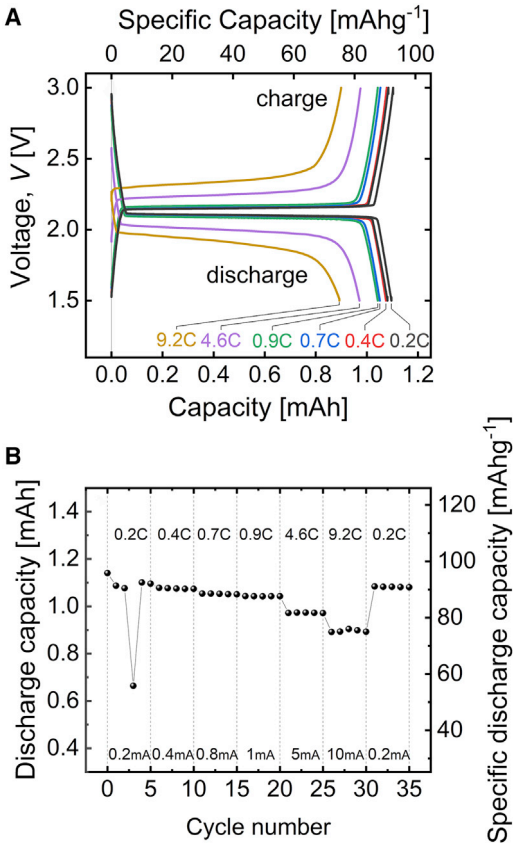

Figure 4. Battery characterization

(A) Charge-discharge curves of the NaTi2(PO4)2 @CNF/DEGDME/Na with specific capacity on the secondary x axis.

(B) The rate capability of the cell at the respective charge rates up to 10 mA (9.2 C-rate) with specific capacity on the secondary y axis.

$$C = \frac{P_{wp}}{P_{MPP}} \qquad \text{(Equation 1)}$$

of the system refers to the proportion of the operational working power of the solar module/cell compared with the maximum power point output and shows how close to maximum output the solar cell is working at.

Here, P_{wp} refers to the power at the working point of the coupled system with respect to the solar module at a specific irradiance, while P_{MPP} is the maximum power point of the solar module under the same irradiance. It is useful to note that the power into the battery and the power out of the solar cell can be considered the same in directly coupled systems with properly designed contacts. In directly coupled systems, the working point during charging is determined by the intersection of the IV characteristics of the PV module with the battery IV characteristics.[38] Voltage of the battery therefore determines the working point of the PV-battery device, stabilizing it in the absence of power electronics such as MPP trackers.

The PV charging efficiency is defined as

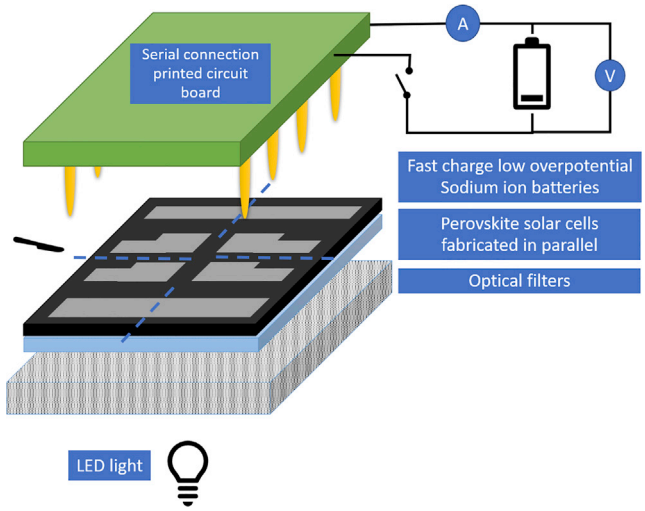

Figure 5. Schematic for experiment

Illustration of how the test was performed using the cut cells and how they were connected in series by the printed circuit board. Illumination intensity was attenuated by using a series of neutral density filters.

$$\eta_{\mathrm{PV-to-batt}}(\%) = \frac{V_c I_c}{A \times F_x \times P_{light}}, \qquad \text{(Equation 2)}$$

where V_c and I_c are the charging voltage (V) and current (mA) of the battery, respectively. P_{light} is the incident light power density under AM1.5G conditions (100 mW cm^{-2}) or LED lamp (24.5 mW cm^{-2}, cool white 4,000 K color temperature), F_x is the filter attenuation factor for the filter used, and A is the effective area of the solar module (cm^2). The filter attenuation factor is calculated by dividing the short circuit current of the solar module under the filter by the unfiltered LED value. For AM1.5G conditions, no filters were used, and $F_x = 1$. The combined performance of the PV-battery system is thus defined by the metrics as described in our previous work[25] but attenuated by filters.

Battery round-trip efficiency

$$\eta_{\mathrm{round-trip}}(\%) = \frac{E_d}{E_c} = \frac{\int_{t_{d,start}}^{t_{d,\,end}} P_d \mathrm{d}t_d}{\int_{t_c,start}^{t_c,end} P_c \mathrm{d}t_c} \qquad \text{(Equation 3)}$$

is the fraction of energy stored in the battery that can be extracted for that cycle.[47] E_d is the energy from the battery on discharge, and E_c is the energy charged into the battery from the solar module. It is defined as the integral of the battery power curve during discharge (P_d) with respect to discharge time (t_d) over the integral of the battery power curve during charging ($P_c = I_c \times V_c$) with respect to the charging time (t_c).

Overall efficiency

$$\eta_{\mathrm{overall}}(\%) = \eta_{\mathrm{round-trip}} \times \eta_{\mathrm{PV-to-batt}} \qquad \text{(Equation 4)}$$

is the product of the solar charging efficiency with the battery round-trip efficiency.[27–29] It represents the overall efficiency of the system in capturing, storing, and subsequently providing that energy for use. It should be noted that it is only valid for relatively unchanging voltages, negligible changes to the battery state of

Table 1. Intensities in lux and SI units for the filtered and non-filtered LED illumination for the charge-discharge measurements

Filter values	Measured intensity [lx]	Measured intensity [Wm^{-2}]
no filter	76,702.29	245.381
0.6713	49,412.23	157.585
0.3821	27,775.69	88.543
0.0108	803.262	2.566
0.0070	518.477	1.651
0.0045	308.367	0.982

charge, or short periods of time. For longer periods or fluctuating conditions, time averaging of Equation 2 or taking the time integral of power incident in place of instantaneous values in Equation 2 gives the following form:

$$\eta_{\text{overall}}(\%) = \frac{E_d}{(F_x \cdot P_{light}) \times A \times t_c} \times 100\% = \frac{\int_{t_{d,start}}^{t_{d,\ end}} P_d \, dt_d}{A \times \left(F_x \int_{t_c,start}^{t_c,end} (P_{light}) dt_c\right)} \times 100\%. \quad \text{(Equation 5)}$$

DISCUSSION

Given that the battery and solar module are directly coupled, the working points of the coupled system correspond to the intersection of the respective IV curves of both devices. The illustrative approximate battery IV curve is plotted using the last working point during charging at the respective illumination intensities of the solar module in Figure 6A. In Figure 6A, we overlay the battery IV curve with the IV curve of the solar module under various levels of LED illumination by plotting the working points on the solar module IVs. The IV curve of the battery only shows slight impact of the voltage along with higher current. The voltage increases from 2.11 (0.03 mA) to 2.16 V (1.56 mA). This resembles a straight line given the high rate capability and low overpotential of the sodium-ion battery.

In Figure 6B, open-circuit voltages, MPP voltages, working voltages of the perovskite module, and battery open-circuit voltages are plotted against the short-circuit current density of the perovskite module, as a proxy for LED light intensity. For our solar module, the blue shaded region represents the approximate light intensity we designed this pairing of solar module and battery combination to work best at (300–500 lux). This region corresponds to an LED irradiance of 0.098–0.165 $mWcm^{-2}$.

The solar module voltages can be seen to follow a log-linear decrease with decreasing intensity. This gives a good correlation to the equations for ideality factor of a PSC in literature found by varying the open-circuit voltage of a solar cell with varying incident photon flux,[48–51]

$$V_{\text{OC module}} = 3 \times V_{\text{OC Cell}} + constant = 3(n_{id})\left(\frac{kT}{q}\right)\ln\left(\frac{J_{SC}}{J_0}\right) + constant, \quad \text{(Equation 6)}$$

where n_{id} is the ideality factor and J_0 is the saturation current density. The thermal voltage is given by kT/q (sometimes denoted as V_T), where kT is the thermal energy, q is elemental charge, and k is the Boltzmann constant. The ideality factor for the module is approximately 1.83 (supplemental information; Figure S5). This value above 1.5 indicates that the band alignment is very favorable, with recombination mainly stemming from interfacial recombination.[51]

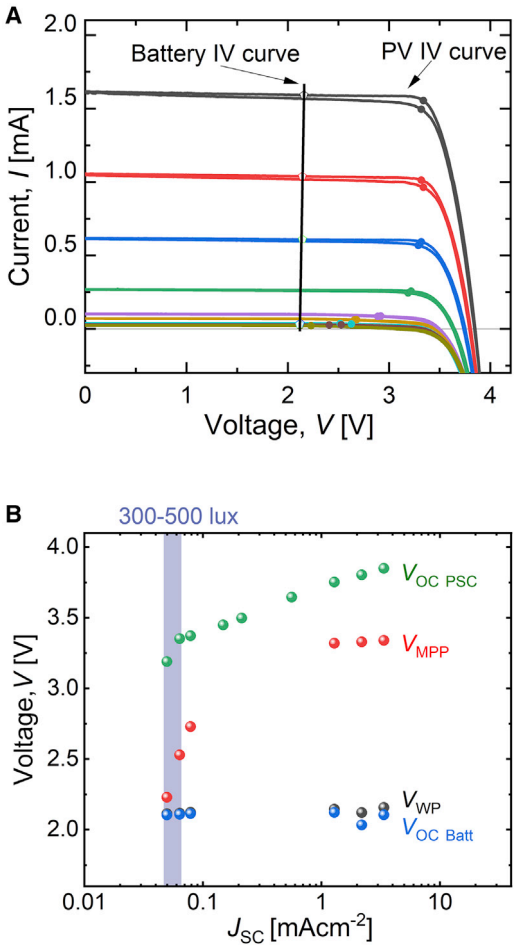

Figure 6. Voltages and short-circuit current density of the coupled system

(A) Current-voltage (IV) curves of the three-cell $CH_3NH_3Pb(I_{0.8}Br_{0.2})_3$ module with CMC:ICBA ETL, with maximum power points, overlaid with the battery charging points at the respective working points under LED illumination with various applied filters. The dark gray curve is without filters applied. The almost vertical black line approximates the battery IV curve for our experiments.

(B) Perovskite solar module open-circuit voltage ($V_{oc\ PSC}$), maximum power point voltage (V_{MPP}), system voltage during direct battery charging (V_{wp}), and battery open-circuit voltage ($V_{oc\ Batt}$) plotted against the short circuit current density of the solar module as a proxy for light intensity.

There are different either approximate or implicit relations for V_{mpp} in the literature that are valid under different circumstances,[52,53] and V_{mpp} usually follows a similar trend to that of V_{oc}, but this is not the case for our data. We postulate that there might be a shunt in one of the cells that becomes more prominent at lower currents and results in a steep drop off of fill factor at lower intensity. The divergence of V_{mpp} with V_{oc} at higher currents is most likely due to a typical effect of the series resistance becoming more dominant at higher currents as is consistent with concentrator perovskite cells under one-sun irradiance.[54]

The V_{MPP} of the perovskite solar module is always higher than the charging voltage of the battery even at 300–500 lux illumination. Because the working point of the module is tied to the voltage of the battery and the charge rates under LED illumination are under 1C rate, the setup charges at approximately 2.13 V regardless of

Please cite this article in press as: Kin et al., Efficient indoor light harvesting with $CH_3NH_3Pb(I_{0.8}Br_{0.2})_3$ solar modules and sodium-ion battery, Cell Reports Physical Science (2022), https://doi.org/10.1016/j.xcrp.2022.101123

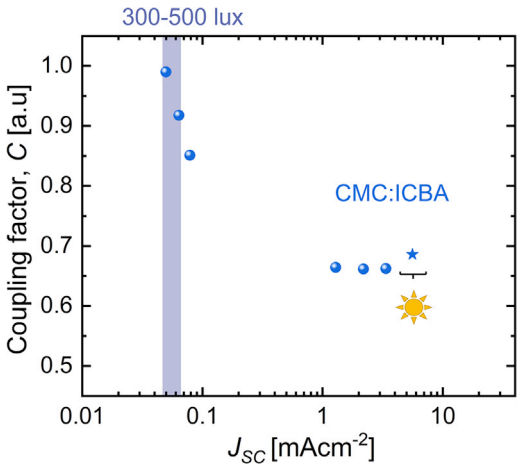

Figure 7. Coupling factor versus short-circuit current density under LED illumination

Coupling factor for AM1.5G charging is indicated by the star and highlighted.

intensity. Thus, we have a minimum charging power of approximately 135 μW cm^{-2} under the densest filter used for charging at around 300–500 lux.

In Figure 7, the coupling factor is plotted versus short-circuit current density (J_{sc}) for the $CH_3NH_3Pb(I_{0.8}Br_{0.2})_3$ modules. The modules are designed to provide sufficient voltage to the battery under typical office lighting conditions and thus has a high coupling factor (of 0.91–0.98) in our target range of 300–500 lux. An increase in illumination intensity leads to the increase in the MPP voltage and related reduction of the coupling factor—V_{MPP} departs from the nearly constant working point voltage following Equation 6. This is seen in Figure 7A, where coupling factor plateaus to 0.66 (Figure 7B) without filters. This is comparable to the coupling factor under AM1.5G (stars in Figure 7) of 0.68.

The flat charging plateau of the battery is the cause of this unchanging coupling factor with time (see Figures S6 and S7). The nearly constant working point of the solar cell enables us to avoid analysis of the state of charge of the battery. If a commercial Li-ion battery were to be used, the cell voltage will change with the state of charge of the cell across a wide range of voltages, complicating our system analysis by changing the working point depending on the state of charge of the battery and the rate at which the coupling factor changes during charging.

Next, we plot the module efficiency under LED illumination (η_{LED}), battery charging efficiency ($\eta_{PV\text{-}to\text{-}batt}$), and overall system efficiency ($\eta_{overall}$) versus short-circuit current density (J_{sc}) (Figure 8). We also plot the same respective efficiencies under one-sun illumination (stars) as reference. Under LED illumination, we achieved a maximum module efficiency of 43.9% and a minimum of 31%. Compared with the module efficiency under AM1.5G illumination of approximately 18%, this value is exceptional. The excellent performance under LED illumination can be attributed to good matching between the LED light spectrum and the quantum efficiency (QE) of the PSC—the result of the wide band gap of the $CH_3NH_3Pb(I_{0.8}Br_{0.2})_3$ layer, which is in line with previous theoretical studies.[23]

Charging efficiencies ($\eta_{PV\text{-}to\text{-}batt}$) were all above 20% under LED illumination regardless of intensity. The extremely low overpotentials of the battery meant that overall energy loss from storage was minimized, thus overall efficiencies ($\eta_{overall}$) track the charging efficiencies closely even at high intensities. Coupled

Please cite this article in press as: Kin et al., Efficient indoor light harvesting with $CH_3NH_3Pb(I_{0.8}Br_{0.2})_3$ solar modules and sodium-ion battery, Cell Reports Physical Science (2022), https://doi.org/10.1016/j.xcrp.2022.101123

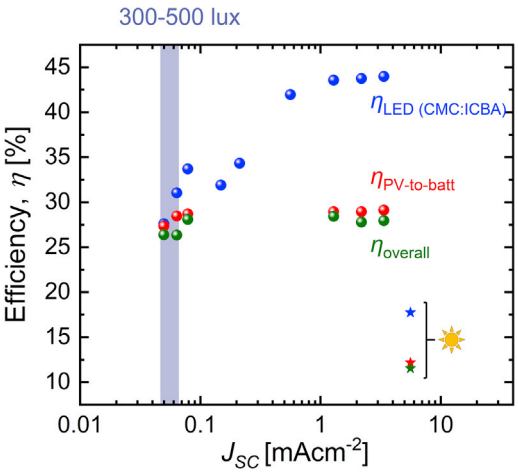

Figure 8. Module efficiency (η_{LED}), charging efficiency ($\eta_{PV\text{-}to\text{-}batt}$), and overall efficiency ($\eta_{overall}$) versus short-circuit current density of the solar module under LED illumination

300–500 lux LED intensity has been highlighted in blue gray. AM1.5G results have been plotted as stars for comparison.

with the much higher module efficiencies under LED illumination than under AM1.5G, overall efficiencies ranged from 26.3% to 27.9%, which is more than double the value under AM1.5G illumination (11.5%). We found that overall efficiency across a wide range of illumination remained relatively constant, as the operating voltage is conservatively planned to be at a lower voltage, and so efficiency was unaffected by the voltage drop due to the decrease in illumination. Our results thus also experimentally show that with the right battery combination, the flat dependence of the efficiency of PV-battery combination observed for both PV modules is in line with predictions of our previous study.[38] Note that under high LED intensity, a two-cell module can be applied. However, in our combination of solar cell and battery technologies, the three-cell module provides the best coupling under target illumination range.

It is interesting to note that the fullerene blend ETL was optimized for AM1.5G operation,[22] but its performance under LED operation is thus far unexplored. More exploratory work needs to be done to see if other ETLs that give higher currents under AM1.5G also give the same performance under LED illumination.

The losses in our setup mainly relate to power coupling. Coupling losses are low in the 300–500 lux range, as the PV-battery combinations were designed to operate under this intensity. Given that the fixed 2 kΩ resistor is used to discharge the battery after charging, a similar area specific load resistance (based on battery electrode area) of 1.76 kΩcm^{-2} for sensors and other electronics will perform similarly to our results. The discharge current under the fixed resistor is typically 0.9–1 mA at 2.05–2.1 V, giving a power output of approximately 2 mW. The maximum charge power we have achieved under 300 lux of 2.1 mW (CMC:ICBA) under high-intensity LED illumination (24.5 mW cm^{-2}) may not seem high enough to power modern electronics; however, it should be noted that the maximum discharge capability of the battery is ~18 mWcm^{-2} and should be sufficient for most sensors or applications with infrequent high pulsed loads.

In conclusion, we demonstrate high-efficiency light harvesting under a wide range of indoor LED illumination intensities using a wide-band-gap perovskite PV module. We have coupled the $CH_3NH_3Pb(I_{0.8}Br_{0.2})_3$ module to a high-rate-capable

sodium-ion battery to achieve overall efficiencies in excess of 24% under LED. The device is also capable of safe operation under AM1.5G illumination.

We report a maximum power conversion efficiency of a wide-band-gap lead halide perovskite solar module of 43.9% under concentrated LED illumination (24.5 $mWcm^{-2}$) and 31% under 500 lux. For a non-integrated, directly coupled PV-battery system, a record efficiency for PV charging under 500 lux LED illumination ($\eta_{LED\text{-}to\text{-}batt}$ = 28.5%) was also achieved, with a corresponding high efficiency under reference AM1.5G illumination ($\eta_{solar\text{-}to\text{-}batt}$ = 12.2%). These respective illumination charging efficiencies resulted in a record overall efficiency($\eta_{overall}$) of 26.4% (under 500 lux LED) and 11.5% (under AM1.5G).

This is the first time a perovskite-charged battery is shown to operate at both one-sun illumination as well as indoor lighting conditions with high efficiency throughout the whole range of illumination from indoor to outdoor conditions. The high efficiencies under indoor LED illumination can be directly attributed to the wide-band-gap PSCs and the good alignment of the solar module QE with the LED spectrum. The use of a high-rate-capability sodium-ion battery technology with low charge-discharge overpotential enabled effective storage of energy and the possibility to power low-voltage electronics with much higher stability and power. This combination allowed us to achieve overall efficiencies above 23% regardless of LED illumination intensity.

The combination of a wide-band-gap perovskite module and a sodium-ion battery represents promising power solution for variety of upcoming indoor electronics. One notable feature of this combination is high charge-rate capability of the sodium-ion battery, which ensures safe operation even if the light harvester is exposed to direct sun. Furthermore, the high rate capability of the battery also enables high pulse current discharge without damaging the cell, which will be useful for transmission and antenna operation for internet-of-things applications.[55] The reduced losses from battery overpotential resulting in an 11.5% overall efficiency under AM1.5G is also an improvement relative to our previous work[25] and is in line with the previously predicted boost in efficiency with the elimination of the converter and using a battery capable of much higher current densities, thus reducing battery-related storage losses.

Being a much more widely available metal, sodium-ion technology also is better poised to provide cheap and widespread adoption in internet-of-things applications such as distributed indoor sensor networks. The use of diglyme with metallic sodium anodes charging under current densities in excess of 1 $mAcm^{-1}$ is also noteworthy, and this threshold was exceeded under concentrated LED as well as under AM1.5G conditions. It should also be noted that the same cell was used for all tests under AM1.5 and LED charging and is a testament to the stability of the chemistry. The small physical size of both the solar module (0.48 cm^2) and the battery (1.13 cm^2) show the potential for scaling as long as the current densities of the solar module remain within the material limits of the battery.

Future work to possibly tailor an ETL and absorber layer specifically for LED illumination may further increase the efficiency closer to the theoretical maximum of more than 57% for a band gap of 1.82 eV.

Please cite this article in press as: Kin et al., Efficient indoor light harvesting with $CH_3NH_3Pb(I_{0.8}Br_{0.2})_3$ solar modules and sodium-ion battery, Cell Reports Physical Science (2022), https://doi.org/10.1016/j.xcrp.2022.101123

EXPERIMENTAL PROCEDURES

Resource availability

Lead contact

Further information and requests for resources and materials should be directed to and will be fulfilled by the lead contact, Dr. Tsvetelina Merdzhanova (t.merdzhanova@fz-juelich.de).

Materials availability

The materials in this study will be made available on request.

Data and code availability

All data supporting the findings in this paper are presented in the article and the supplemental information. Any additional information required to reanalyze the data reported in this paper is available from the lead contact upon request.

Materials

Methylammonium iodide (MAI) and methylammonium bromide (MABr) were purchased from Greatcell Solar. Lead acetate ($Pb(CH_3COO)_2$, >98.0%), BCP (>99.0%), and CMC were purchased from TCI. Poly[bis (4-phenyl)(2,4,6-trimethylphenyl)amine] (PTAA; Mn = 17,900, Mw = 33,000) was purchased from purchased from Xi'an Polymer Light Technology Corp (China). ICBA was purchased from Solenne (Groningen, the Netherlands). Toluene (99.8%), N,N-dimethylformamide (DMF; 99.8%), and chlorobenzene (CB; 99.8%) were purchased from Sigma-Aldrich and used as received. All other materials were purchased from Sigma-Aldrich and used as received.

PSC device fabrication

The device fabrication process, statistical breakdown of performance, control devices, and stability tests have been reported in our previous work.[22] For the reader's convenience, we describe the fabrication process here again.

The prepatterned ITO substrates (2.0 × 2.0 cm^2) were bought from Advanced Election Technology and ultrasonically cleaned with soap (Hellmanex III), deionized water, acetone, and IPA in succession for 10 min. The as-cleaned ITO substrates were treated with oxygen plasma (Diener Zepto, 50 W) for 12 min and transferred to an N_2-filled glovebox. 80 μL 75°C PTAA (2.0 mg mL^{-1} in toluene) solution was spin coated onto the ITO substrates with a two-consecutive-step program at 500 RPM for 4 s (with a ramping rate of 500 RPM s^{-1}) and 4,500 RPM for 20 s (with a ramping rate of 800 rpm s^{-1}), then the samples were thermally annealed at 100°C for 10 min and afterward cooled down to room temperature. The perovskite precursor solution prepared by mixing $Pb(CH_3COO)_2$ (0.6 M), MAI (1.485 M), and MABr (0.36 M) in DMF was stirred at room temperature for 24 h and filtered with a 0.45 μm PTFE filter prior to use. To fabricate the perovskite layer, 120 μL perovskite precursor solution was spin coated on the top of PTAA layer by a two-consecutive-step program at 1,400 RPM for 15 s (with a ramping rate of 350 RPM s^{-1}) and 6,000 RPM for 20 s with a ramping rate of 767 RPM s^{-1}. The samples were immediately annealed on a hotplate at 75°C for 2 min. Afterward, they were cooled down to room temperature, and a CMC/ICBA blend solution (60 μL, preheated to 75°C, 10 mg mL^{-1} in CB) was spin coated on the top of perovskite layer at a speed of 1,200 RPM for 60 s (with a ramping rate of 400 RPM s^{-1}) for high V_{oc} PSCs. Finally, BCP (8 nm) and Ag (80 nm) were thermally evaporated sequentially in a separate vacuum chamber (<5 × 10^{-6} Pa).

Battery electrode preparation

Battery electrode preparation was largely based on previous work by Yu et al.[40] with optimizations to further reduce preparation time.

A4-sized CNFs with a thickness of 115 μm were obtained from Tortech Nano-Fibers (Ma'alot-Tarshiha, Israel). The CNFs were cleaned with concentrated hydrochloric acid and a mixture of ethanol/water (1: 1, v/v) several times before use in order to remove surface impurities. All other chemical reagents (of analytical grade) were purchased from Sigma-Aldrich and used as received.

A NaTi–P–O precursor solution was prepared by the dropwise addition of titanium(iv) isopropoxide (~0.05 mol) to ammonium hydroxide (30 mL) under constant vigorous stirring until a white gelatinous precipitate formed. The precipitate was washed with 500 mL deionized water to remove excess base and then dissolved in a 1 M solution of oxalic acid (200 mL) at 60°C under stirring until a transparent solution containing $H_2[TiO(C_2O_4)_2]$ was formed. Sodium acetate (5% stoichiometric excess) and a stoichiometric amount of ammonium dihydrogen phosphate were dissolved in water separately and then added slowly to the transparent solution. The final solution was transparent and slightly cloudy but does not settle after long periods.

The pretreated CNFs were cut into 10 × 10 cm squares, and the precursor solution (1mL) was uniformly drop coated onto the squares using a micropipette and dried at 100°C under vacuum for 2 h in a drying oven. This step was repeated two more times to achieve the desired final mass loading. The coated CNFs were then annealed at 800°C for 8 h in a tube furnace under Ar flow (~20 sccm). NTP@CNF electrodes were obtained after the removal of the loosely bound powders on their surface by uniaxially pressing at 30 MPa in a polyethylene Ziplock bag. The thickness of the prepared electrodes was around 130 μm, and the mass loading of both electrodes was greater than 7.5 mg cm^{-2}. The electrode sheets were then dried under vacuum in a Buchi oven for at least 2 h at 120°C before being transferred to the glove box *in vacuo* for punching and battery assembly.

Battery assembly

The electrochemical properties of the prepared electrodes were assessed in steel Swagelok cells with mylar liners. The assembly of all the test cells was carried out in an Ar-filled glovebox, where the concentrations of water and oxygen were kept at less than 0.1 ppm. The 12 mm diameter electrodes (1.13 cm^2) were cut directly from the prepared sheets, weighed, and then used without further modification. Metallic sodium foil was used as the counter electrode and pressed onto 11 mm nickel discs. Batteries were made with 1 M $NaPF_6$ in 2-methoxyethyl ether (DEGDME, or diglyme) electrolyte and glass fiber (Whatmann, GF1) separators. Electrolyte was dried with molecular sieve at least 1 day after preparation and kept with molecular sieve in a sealed bottle within the glove box thereafter to eliminate any trace water content, which was essential to ensure reproducible results.

Three-terminal PV-battery test setup

The setup used is the same setup as previously reported[25] with the exception that the boost converter is removed and that connection shorted. The solar module is not encapsulated but is housed in an airtight measurement box with dry nitrogen atmosphere with quartz window and is linked to the battery via a relay box and Keithley signal measurement units acting as ammeter and voltmeter, which is then connected to a separate switch box with a 2 kΩ resistor and Keithley signal measurement units for

voltage and current measurements. This setup allows for the disconnection of the solar module from the battery for standalone solar cell testing or standalone discharge of the battery across the resistor. Data are logged in real time, and all switches and signal measurement units are controlled by custom software built in-house.

All solar-battery charging tests under AM1.5G illumination (AM1.5G spectrum, 100 mW cm^{-2}) were done using a class-A sun simulator from Wacom. Further details on AM1.5G calibration can be found in Figures S4 and S10. LED charging tests were performed in the same setup with the sun simulator replaced by an Osram 5.5W PAR16 GU10 LED spotlight (4000 K), 20 cm from the module aperture. LED intensity and spectrum were measured using a spectral analyzer before each set of measurements after at least 15 min from turning on the bulb to allow for stabilization. Neutral density filters of 20 × 20 cm sandwiched between glass were used to attenuate the LED intensity down to the required levels. The battery was charged for a minimum of 60 s and to a maximum of 600 s depending on the intensity of illumination. The battery was discharged across the 2 kΩ resistor during discharge for variable times depending on the amount of charge accumulated during charging. All IV scans were done with no dwell time, a 20 ms integration time per step, at 0.02 V/step (1V/s sweep rate).

SUPPLEMENTAL INFORMATION

Supplemental information can be found online at https://doi.org/10.1016/j.xcrp.2022.101123.

ACKNOWLEDGMENTS

The writers would like to thank Daniel Weigand and Jürgen Radde for their help in crafting the custom PCB and Benjamin Klingebiel for his help with the measurement box retrofitting. Christoph Zahren is acknowledged for setting up, calibrating, and maintaining the measuring system and spectral measurements. The authors acknowledge the HITEC fellowship program for funding.

AUTHOR CONTRIBUTIONS

Conceptualization, L.-C.K., O.A., and T.M.; data curation, L.-C.K. and Z.L.; formal analysis, L.-C.K. and S.S.; investigation, L.-C.K. and Z.L.; methodology, L.-C.K. and Z.L.; validation, L.-C.K., Z.L., and O.A.; visualization, L.-C.K. and S.S.; writing – original draft, L.-C.K., Z.L., and T.K.; writing – review & editing, L.-C.K., Z.L., O.A., H.K., T.K., and T.M.; supervision, H.K., T.K., R.-A.E., U.R., and T.M.; resources, T.K., R.-A.E., and U.R.; funding acquisition, T.K., R.-A.E., U.R., and T.M.; project administration, T.K. and T.M.

DECLARATION OF INTERESTS

The authors declare no competing interests.

INCLUSION AND DIVERSITY

One or more of the authors of this paper self-identifies as an underrepresented ethnic minority in science. We support inclusive, diverse, and equitable conduct of research.

Received: July 6, 2022
Revised: September 2, 2022
Accepted: October 7, 2022
Published: November 1, 2022

REFERENCES

1. Zissis, G., Bertoldi, P., and Serrenho, T. (2021). Update on the Status of LED-Lighting World Market since 2018 European Commission. 2021. https://publications.jrc.ec.europa.eu/repository/bitstream/JRC122760/status_of_led_lighting_world_market_2020_final_rev_2.pdf.

2. Peleg, R. (2021). Saule Technologies Launches Electronic Shelf Labels Powered by Perovskite Solar Cells. https://www.perovskite-info.com/saule-technologies-launches-electronic-shelf-labels-powered-perovskite-solar.

3. Olzhabay, Y., Ng, A., and Ukaegbu, I.A. (2021). Perovskite PV energy harvesting system for uninterrupted IoT device applications. Energies *14*, 7946.

4. Tsai, T., and Chen, K. (2013). A 3.4mW photovoltaic energy-harvesting charger with integrated maximum power point tracking and battery management. In 2013 IEEE International Solid-State Circuits Conference Digest of Technical Papers (IEEE).

5. Agbo, S.N., Merdzhanova, T., Rau, U., and Astakhov, O. (2017). Illumination intensity and spectrum-dependent performance of thin-film silicon single and multijunction solar cells. Sol. Energy Mater. Sol. Cell. *159*, 427–434. https://doi.org/10.1016/j.solmat.2016.09.039.

6. Chime, U., Wolf, L., Buga, V., Weigand, D., Gad, A., Köhler, J., Lambertz, A., Duan, W., Ding, K., Merdzhanova, T., et al. How thin practical silicon heterojunction solar cells could be? experimental study under 1 sun and under indoor illumination. Solar RRL *6*, 2100594. https://doi.org/10.1002/solr.202100594.

7. Shockley, W., and Queisser, H.J. (1961). Detailed balance limit of efficiency of p-n junction solar cells. J. Appl. Phys. *32*, 510–519. https://doi.org/10.1063/1.1736034.

8. Lübke, D., Hartnagel, P., Angona, J., and Kirchartz, T. (2021). Comparing and quantifying indoor performance of organic solar cells. Adv. Energy Mater. *11*, 2101474. https://doi.org/10.1002/aenm.202101474.

9. Almora, O., Baran, D., Bazan, G.C., Berger, C., Cabrera, C.I., Catchpole, K.R., Erten-Ela, S., Guo, F., Hauch, J., Ho-Baillie, A.W.Y., et al. (2021). Device performance of emerging photovoltaic materials (Version 2). Adv. Energy Mater. *11*, 2102526. https://doi.org/10.1002/aenm.202102526.

10. Cui, Y., Xu, Y., Yao, H., Bi, P., Hong, L., Zhang, J., Zu, Y., Zhang, T., Qin, J., Ren, J., et al. (2021). Single-junction organic photovoltaic cell with 19% efficiency. Adv. Mater. *33*, 2102420. https://doi.org/10.1002/adma.202102420.

11. Yoo, J.J., Seo, G., Chua, M.R., Park, T.G., Lu, Y., Rotermund, F., Kim, Y.-K., Moon, C.S., Jeon, N.J., Correa-Baena, J.-P., et al. (2021). Efficient perovskite solar cells via improved carrier management. Nature *590*, 587–593. https://doi.org/10.1038/s41586-021-03285-w.

12. Jeong, J., Kim, M., Seo, J., Lu, H., Ahlawat, P., Mishra, A., Yang, Y., Hope, M.A., Eickemeyer, F.T., Kim, M., et al. (2021). Pseudo-halide anion engineering for α-FAPbI3 perovskite solar cells. Nature *592*, 381–385. https://doi.org/10.1038/s41586-021-03406-5.

13. Min, H., Lee, D.Y., Kim, J., Kim, G., Lee, K.S., Kim, J., Paik, M.J., Kim, Y.K., Kim, K.S., Kim, M.G., et al. (2021). Perovskite solar cells with atomically coherent interlayers on SnO2 electrodes. Nature *598*, 444–450. https://doi.org/10.1038/s41586-021-03964-8.

14. Kim, M., Jeong, J., Lu, H., Lee, T.K., Eickemeyer, F.T., Liu, Y., Choi, I.W., Choi, S.J., Jo, Y., Kim, H.-B., et al. (2022). Conformal quantum dot-SnO_2 layers as electron transporters for efficient perovskite solar cells. Science *375*, 302–306. https://doi.org/10.1126/science.abh1885.

15. Jacobsson, T.J., Hultqvist, A., García-Fernández, A., Anand, A., Al-Ashouri, A., Hagfeldt, A., Crovetto, A., Abate, A., Ricciardulli, A.G., Vijayan, A., et al. (2022). An open-access database and analysis tool for perovskite solar cells based on the FAIR data principles. Nat. Energy *7*, 107–115. https://doi.org/10.1038/s41560-021-00941-3.

16. Cutting, C.L., Bag, M., and Venkataraman, D. (2016). Indoor light recycling: a new home for organic photovoltaics. J. Mater. Chem. C Mater. *4*, 10367–10370. https://doi.org/10.1039/C6TC03344J.

17. Cheng, R., Chung, C., Zhang, H., Liu, F., Wang, W., Zhou, Z., Wang, S., Djurišić, A.B., and Feng, S. (2019). Tailoring triple-anion perovskite material for indoor light harvesting with restrained halide segregation and record high efficiency beyond 36. Adv. Energy Mater. *9*, 1901980. https://doi.org/10.1002/aenm.201901980.

18. Li, M., Igbari, F., Wang, Z., and Liao, L. (2020). Indoor thin-film photovoltaics: progress and challenges. Adv. Energy Mater. *10*, 2000641. https://doi.org/10.1002/aenm.202000641.

19. Liu, Z., Krückemeier, L., Krogmeier, B., Klingebiel, B., Márquez, J.A., Levcenko, S., Öz, S., Mathur, S., Rau, U., Unold, T., and Kirchartz, T. (2019). Open-circuit voltages exceeding 1.26 V in planar Methylammonium lead iodide perovskite solar cells. ACS Energy Lett. *4*, 110–117. https://doi.org/10.1021/acsenergylett.8b01906.

20. Krückemeier, L., Liu, Z., Krogmeier, B., Rau, U., and Kirchartz, T. (2021). Consistent interpretation of electrical and optical transients in halide perovskite layers and solar cells. Adv. Energy Mater. *11*, 2102290. https://doi.org/10.1002/aenm.202102290.

21. Krückemeier, L., Krogmeier, B., Liu, Z., Rau, U., and Kirchartz, T. (2021). Understanding transient photoluminescence in halide perovskite layer stacks and solar cells. Adv. Energy Mater. *11*, 2003489. https://doi.org/10.1002/aenm.202003489.

22. Liu, Z., Siekmann, J., Klingebiel, B., Rau, U., and Kirchartz, T. (2021). Interface optimization via fullerene blends enables open-circuit voltages of 1.35 V in CH3NH3Pb(I0.8Br0.2)3 solar cells. Adv. Energy Mater. *11*, 2003386. https://doi.org/10.1002/aenm.202003386.

23. Ho, J.K.W., Yin, H., and So, S.K. (2020). From 33% to 57% – an elevated potential of efficiency limit for indoor photovoltaics. J. Mater. Chem. A Mater. *8*, 1717–1723. https://doi.org/10.1039/C9TA11894B.

24. Freunek, M., Freunek, M., and Reindl, L.M. (2013). Maximum efficiencies of indoor photovoltaic devices. IEEE J. Photovolt. *3*, 59–64. https://doi.org/10.1109/JPHOTOV.2012.2225023.

25. Kin, L.-c., Liu, Z., Astakhov, O., Agbo, S.N., Tempel, H., Yu, S., Kungl, H., Eichel, R.-A., Rau, U., Kirchartz, T., and Merdzhanova, T. (2019). Efficient area matched converter aided solar charging of lithium ion batteries using high voltage perovskite solar cells. ACS Appl. Energy Mater. *3*, 431–439. https://doi.org/10.1021/acsaem.9b01672.

26. Kim, Y., Seo, H., Kim, E., Kim, J., and Seo, I. (2020). Development of a self-charging lithium-ion battery using perovskite solar cells. Nanomaterials *10*, 1705.

27. Xu, J., Chen, Y., and Dai, L. (2015). Efficiently photo-charging lithium-ion battery by perovskite solar cell. Nat. Commun. *6*, 8103. https://doi.org/10.1038/ncomms9103.

28. Chen, P., Li, T.-T., Yang, Y.-B., Li, G.-R., and Gao, X.-P. (2022). Coupling aqueous zinc batteries and perovskite solar cells for simultaneous energy harvest, conversion and storage. Nat. Commun. *13*, 64. https://doi.org/10.1038/s41467-021-27791-7.

29. Hu, Y., Bai, Y., Luo, B., Wang, S., Hu, H., Chen, P., Lyu, M., Shapter, J., Rowan, A., and Wang, L. (2019). A portable and efficient solar-rechargeable battery with ultrafast photo-charge/discharge rate. Adv. Energy Mater. *9*, 1900872. https://doi.org/10.1002/aenm.201900872.

30. He, X., Chen, J., Ren, X., Zhang, L., Liu, Y., Feng, J., Fang, J., Zhao, K., and Liu, S.F. (2021). 40.1% record low-light solar-cell efficiency by holistic trap-passivation using micrometer-thick perovskite film. Adv. Mater. *33*, 2100770. https://doi.org/10.1002/adma.202100770.

31. Castro-Hermosa, S., Lucarelli, G., Top, M., Fahland, M., Fahlteich, J., and Brown, T.M. (2020). Perovskite photovoltaics on roll-to-roll coated ultra-thin glass as flexible high-efficiency indoor power generators. Cell Reports Physical Science *1*, 100045. https://doi.org/10.1016/j.xcrp.2020.100045.

32. Lucarelli, G., Di Giacomo, F., Zardetto, V., Creatore, M., and Brown, T.M. (2017). Efficient light harvesting from flexible perovskite solar cells under indoor white light-emitting diode illumination. Nano Res. *10*, 2130–2145. https://doi.org/10.1007/s12274-016-1402-5.

33. Chen, S., Dai, X., Xu, S., Jiao, H., Zhao, L., and Huang, J. (2021). Stabilizing perovskite-substrate interfaces for high-performance perovskite modules. Science *373*, 902–907. https://doi.org/10.1126/science.abi6323.

34. Ritzer, D.B., Abzieher, T., Basibüyük, A., Feeney, T., Laufer, F., Ternes, S., Richards, B.S., Bergfeld, S., and Paetzold, U.W. (2022). Upscaling of perovskite solar modules: the synergy of fully evaporated layer fabrication and all-laser-scribed interconnections. Progress in Photovoltaics. *30*, 360–373. https://doi.org/10.1002/pip.3489.

35. Opoku, H., Hyeon Lee, J., Won Shim, J., and Woong Jo, J. (2022). Perovskite photovoltaics

for artificial light harvesting. Chemistry – a European journal. Chemistry *28*, e202200266. https://doi.org/10.1002/chem.202200266.

36. Lim, J.W., Kwon, H., Kim, S.H., You, Y.-J., Goo, J.S., Ko, D.-H., Lee, H.J., Kim, D., Chung, I., Kim, T.G., et al. (2020). Unprecedentedly high indoor performance (efficiency > 34 %) of perovskite photovoltaics with controlled bromine doping. Nano Energy *75*, 104984. https://doi.org/10.1016/j.nanoen.2020.104984.

37. Green, M.A., Dunlop, E.D., Hohl-Ebinger, J., Yoshita, M., Kopidakis, N., and Ho-Baillie, A.W. (2020). Solar cell efficiency tables (Version 55). Prog. Photovolt. Res. Appl. *28*, 3–15. https://doi.org/10.1002/pip.3228.

38. Astakhov, O., Merdzhanova, T., Kin, L.-C., and Rau, U. (2020). From room to roof: how feasible is direct coupling of solar-battery power unit under variable irradiance? Sol. Energy *206*, 732–740. https://doi.org/10.1016/j.solener.2020.06.033.

39. Preto, S., and Gomes, C.C. (2019). Lighting in the Workplace: Recommended illuminance (lux) at workplace environs. In Advances in Design for Inclusion. AHFE 2018., *776*, G. Di Bucchianico, ed., Advances in Design for Inclusion. AHFE 2018. (Springer, Cham: Advances in Intelligent Systems and Computing), pp. 180–191. https://doi.org/10.1007/978-3-319-94622-1_18.

40. Yu, S., Liu, Z., Tempel, H., Kungl, H., and Eichel, R.-A. (2018). Self-standing NASICON-type electrodes with high mass loading for fast-cycling all-phosphate sodium-ion batteries. J. Mater. Chem. A Mater. *6*, 18304–18317. https://doi.org/10.1039/C8TA07313A.

41. Khadka, D.B., Shirai, Y., Yanagida, M., Noda, T., and Miyano, K. (2018). Tailoring the open-circuit voltage deficit of wide-band-gap perovskite solar cells using alkyl chain-substituted fullerene derivatives. ACS Appl. Mater. Interfaces *10*, 22074–22082. https://doi.org/10.1021/acsami.8b04439.

42. Chikamatsu, M., Kikuchi, K., Kodama, T., Nishikawa, H., Ikemoto, I., Yoshimoto, N., Hanada, T., Yoshida, Y., Tanigaki, N., and Yase, K. (2001). Out-of-plane and in-plane structures of the cast films of long alkyl chain-linked C60 via phenyl ring. AIP Conf. Proc. *590*, 455–458. https://doi.org/10.1063/1.1420150.

43. Wheeler, S., Bryant, D., Troughton, J., Kirchartz, T., Watson, T., Nelson, J., and Durrant, J.R. (2017). Transient optoelectronic analysis of the impact of material energetics and recombination kinetics on the open-circuit voltage of hybrid perovskite solar cells. J. Phys. Chem. C *121*, 13496–13506. https://doi.org/10.1021/acs.jpcc.7b02411.

44. Fang, Y., Zhang, J., Xiao, L., Ai, X., Cao, Y., and Yang, H. (2017). Phosphate framework electrode materials for sodium ion batteries. Adv. Sci. *4*, 1600392. https://doi.org/10.1002/advs.201600392.

45. Goktas, M., Bolli, C., Buchheim, J., Berg, E.J., Novák, P., Bonilla, F., Rojo, T., Komaba, S., Kubota, K., and Adelhelm, P. (2019). Stable and unstable diglyme-based electrolytes for batteries with sodium or graphite as electrode. ACS Appl. Mater. Interfaces *11*, 32844–32855. https://doi.org/10.1021/acsami.9b06760.

46. Westman, K., Dugas, R., Jankowski, P., Wieczorek, W., Gachot, G., Morcrette, M., Irisarri, E., Ponrouch, A., Palacín, M.R., Tarascon, J.M., and Johansson, P. (2018). Diglyme based electrolytes for sodium-ion batteries. ACS Appl. Energy Mater. *1*, 2671–2680. https://doi.org/10.1021/acsaem.8b00360.

47. Conover, D.R., Crawford, A.J., Viswanathan, V.V., Ferreira, S., and Schoenwald, D. (2014). Protocol for Uniformly Measuring and Expressing the Performance of Energy Storage Systems (Pacific Northwest National Lab(PNNL)).

48. Caprioglio, P., Wolff, C.M., Sandberg, O.J., Armin, A., Rech, B., Albrecht, S., Neher, D., and Stolterfoht, M. (2020). On the origin of the ideality factor in perovskite solar cells. Adv. Energy Mater. *10*, 2000502. https://doi.org/10.1002/aenm.202000502.

49. Calado, P., Burkitt, D., Yao, J., Troughton, J., Watson, T.M., Carnie, M.J., Telford, A.M., O'Regan, B.C., Nelson, J., and Barnes, P.R. (2019). Identifying dominant recombination mechanisms in perovskite solar cells by measuring the transient ideality factor. Phys. Rev. Appl. *11*, 044005. https://doi.org/10.1103/PhysRevApplied.11.044005.

50. Wetzelaer, G.A.H., Kuik, M., Lenes, M., and Blom, P.W.M. (2011). Origin of the dark-current ideality factor in polymer:fullerene bulk heterojunction solar cells. Appl. Phys. Lett. *99*, 153506. https://doi.org/10.1063/1.3651752.

51. Kirchartz, T., and Nelson, J. (2012). Meaning of reaction orders in polymer:fullerene solar cells. Phys. Rev. B *86*, 165201. https://doi.org/10.1103/PhysRevB.86.165201.

52. Green, M.A. (1982). Accuracy of analytical expressions for solar cell fill factors. Sol. Cell. *7*, 337–340. https://doi.org/10.1016/0379-6787(82)90057-6.

53. Taretto, K., Soldera, M., and Troviano, M. (2013). Accurate explicit equations for the fill factor of real solar cells—applications to thin-film solar cells. Prog. Photovolt:. Res. Appl. *21*, 1489–1498. https://doi.org/10.1002/pip.2235.

54. Wang, Z., Lin, Q., Wenger, B., Christoforo, M.G., Lin, Y.-H., Klug, M.T., Johnston, M.B., Herz, L.M., and Snaith, H.J. (2018). High irradiance performance of metal halide perovskites for concentrator photovoltaics. Nat. Energy *3*, 855–861. https://doi.org/10.1038/s41560-018-0220-2.

55. Raj, A., and Steingart, D. (2018). Review—power sources for the internet of things. J. Electrochem. Soc. *165*, B3130–B3136.